CrossMark

Investigation of in-flame soot optical properties in laminar coflow diffusion flames using thermophoretic particle sampling and spectral light extinction

Nathan J. Kempema[1] · Bin Ma[2] · Marshall B. Long[1]

Abstract Soot optical properties are essential to the non-invasive study of the in-flame evolution of soot particles since they allow quantitative interpretation of optical diagnostics. Such experimental data are critical for comparison to results from computational models and soot sub-models. In this study, the thermophoretic sampling particle diagnostic (TSPD) technique is applied along with data from a previous spectrally resolved line-of-sight light attenuation experiment to determine the soot volume fraction and absorption function. The TSPD technique is applied in a flame stabilized on the Yale burner, and the soot scattering-to-absorption ratio is calculated using the Rayleigh–Debye–Gans theory for fractal aggregates and morphology information from a previous sampling experiment. The soot absorption function is determined as a function of wavelength and found to be in excellent agreement with previous in-flame measurements of the soot absorption function in coflow laminar diffusion flames. Two-dimensional maps of the soot dispersion exponent are calculated and show that the soot absorption function may have a positive or negative exponential wavelength dependence depending on the in-flame location. Finally, the wavelength dependence of the soot absorption function is related to the ratio of soot absorption functions, as would be found using two-excitation-wavelength laser-induced incandescence.

✉ Nathan J. Kempema
  nathan.kempema@yale.edu

[1] Department of Mechanical Engineering and Materials Science, Yale University, 15 Prospect St., New Haven, CT 06511, USA

[2] GE Global Research Center, Niskayuna, NY, USA

1 Introduction

Optical properties of soot are important to the study of the in-flame evolution of soot particles in addition to modeling the post-flame effect that soot has on our climate. In the atmosphere, soot particles play a role in climate forcing, and knowledge of their optical properties is crucial to modeling the impact of soot emission on our environment [1]. When studying the in-flame evolution of soot particles, noninvasive laser diagnostics are often utilized to provide high spatially and temporally resolved measurements. However, measurements are limited by the accuracy of the known optical properties, as they are the quantitative link between in-flame soot properties and experimental optical data. Therefore, both the optical study of how soot is produced in-flame and models of the effect it has post-flame are predicated on knowledge of soot optical properties.

This study will investigate the in-flame optical properties of soot through the soot volume fraction (f_v), which is simply the volume occupied by soot per unit volume of space. The soot volume fraction is a focus here because it is the most commonly used parameter for comparison between experiments and computational models [2–5] and can be calculated from relatively simple optical extinction experiments [6–8]. Thus, to provide accurate experimental data in laboratory-scale burners for comparison to numerical models, the optical properties of soot must be well characterized for the specific reacting flow. The Yale laminar coflow diffusion burner [9] is investigated in this work as it has been extensively studied [2, 10–12] and one of the flames stabilized on this burner is a target flame for the international sooting flames workshop [13].

To measure soot optical properties, many studies rely on an independent measurement of soot volume fraction obtained using gravimetric sampling followed by light

extinction (GSLE) [14–18]. In this technique, over-fire soot is captured and passed through a light extinction experiment before being deposited on a filter. The filter yields the mass of soot collected during a known sampled time and under specific flow conditions. Soot volume fraction can then be calculated with knowledge of the soot density. The extinction data are used in conjunction with the soot volume fraction to solve for the dimensionless soot extinction coefficient (K_{ext}), which further depends on the soot scattering-to-absorption ratio ($\rho_{SA}(\lambda)$), the absorption function ($E(m(\lambda))$), the complex index of refraction of soot ($m(\lambda)$), and the wavelength of light (λ). The Rayleigh–Debye–Gans theory for fractal aggregates (RDG-FA) is often used to calculate $\rho_{SA}(\lambda)$ if the soot morphology is known [19–21], which allows the soot absorption function to be determined.

To investigate the optical properties of cooled post-flame soot, as might be found in the atmosphere, Coderre et al. [20] gravimetrically sampled soot from an inverted methane coflow diffusion flame to determine f_v. They conducted a spectrally resolved line-of-sight attenuation (spec-LOSA) measurement on the over-fire soot, calculated $\rho_{SA}(750–450$ nm$) = 0.18$–0.29 using RDG-FA theory, and determined $E(m)$ as a function of wavelength. They found the soot absorption function to be relatively constant for the post-flame soot over the wavelength interval investigated ($E(m) = 0.35 \pm 0.03$ from 450 to 750 nm). Krishnan et al. [21, 22] gravimetrically sampled over-fire soot from large turbulent diffusion flames to calculate soot volume fraction and therefore the soot absorption function through RDG-FA theory. At 515 nm, they found $E(m$ (515 nm)$) = 0.29$ and $\rho_{SA}(515$ nm$) \approx 0.57$ for relatively large aggregates (number of primary particles per aggregate (N_{ave})~400–500, primary particle diameter (d_p)~30–50 nm). The morphology of the post-flame soot investigated in these studies is important as it affects the derived $\rho_{SA}(\lambda)$ [23] and therefore the calculated $E(m)$ for light extinction experiments. In addition, the age and environment of soot particles may affect internal structure (i.e., degree of graphitization), thereby affecting optical properties. Therefore, although post-flame gravimetric sampling has been shown to be an effective independent measure of soot volume fraction, it is unclear that soot optical properties derived from over-fire soot may be used with accuracy for in-flame measurements due to possible differences in particle age and morphology [1, 24].

To eliminate possible errors associated with applying post-flame-derived soot optical properties to in-flame measurements, a few techniques have been developed to directly measure the in-flame soot volume fraction or absorption function. Williams et al. [19] adapted the GSLE technique to include a probe for in-flame extraction of soot and measured K_{ext} in a variety of burners with different fuel sources. The soot absorption function has been measured through nanoscale heat transfer modeling of soot in laser-induced incandescence (LII) experiments. Snelling et al. [25, 26] matched the peak soot temperature in their heat transfer model to experimental data and determined $E(m)$ at 532 and 1064 nm in a laminar coflow diffusion flame. In another study, Beyer and Greenhalgh [27] conducted an LII experiment in vacuum to determine the soot absorption function, since the vacuum environment simplifies the heat transfer model.

LII has shown the ability not only to measure the absolute soot absorption function, but to also measure its relative wavelength dependence through two-excitation-wavelength LII [28]. In this technique, the spatial and temporal distributions of the absorbed laser pulse energies are matched at two excitation wavelengths, allowing for determination of the ratio of the absorption function at those wavelengths. In the initial study, Therssen et al. [28] demonstrated $E(m(532$ nm$))/E(m(1064$ nm$)) \approx 1$ in a non-premixed flame of pure methane. Recent work by Bejaoui et al. [29] showed that $E(m(532$ nm$))/E(m(1064$ nm$)) \approx 1$ in a premixed McKenna burner, which is consistent with Ref. [25, 26] in the Gülder burner. Migliorini et al. [30] used spec-LOSA and thermophoretic sampling/TEM analysis to arrive at the ($E(m(\lambda_1))/E(m(\lambda_2))$) parameter in premixed and non-premixed flames and showed that the ratio is a function of the height above the burner (HAB). They also showed that after a certain particle age along the centerline of the non-premixed flame (i.e., at a certain HAB), $E(m(450$ nm$))/E(m(750$ nm$))$ becomes effectively constant at ≈ 1.1.

In this study, the thermophoretic sampling particle diagnostic (TSPD) [31] is used to provide an in-flame measurement of soot volume fraction, which along with light extinction information and the soot scattering-to-absorption ratio is used to calculate the soot absorption function. Light extinction information is obtained from a previous spec-LOSA experiment [10], and the ratio is calculated in this study using RDG-FA theory with soot size distributions and morphological parameters determined in Ref. [11] through thermophoretic sampling and TEM analysis. Two of the TSPD samples were taken with multiple exposures to ensure that the results are free of growth or oxidation artifacts. The TSPD technique is first validated for calculation of soot volume fraction by comparison to previously published results [31] in the Santoro burner. Image segmentation and relative optical density (ROD) methods are used to calculate the volume of particles per image on the TEM grid using electron microscope analysis. The derived soot absorption function will be shown to be in excellent agreement with previous independent in-flame measurements of the soot absorption function in coflow laminar diffusion flames. The measurements are inconsistent with

commonly used soot absorption functions derived from GSLE measurements of post-flame soot from turbulent diffusion flames.

The available data sets for the soot dispersion exponent (α), which characterizes the wavelength dependence of the soot absorption function, are extended to other flow conditions (compared to Ref. [10]) stabilized on the Yale burner by showing that the wavelength dependence of the scattering correction to the fitted light extinction data can be approximated as constant over the flame with negligible additional uncertainty. We will show that the derived α maps are in excellent agreement with available two-excitation-wavelength LII data over a wavelength interval of 450–700 nm and can yield a positive or negative exponential soot absorption function wavelength dependence that depends on the in-flame location. The α maps extend the relative absorption function discussion by providing two-dimensional information and demonstrating that the ratio of soot absorption functions is approximately constant for mature centerline aggregates but may change wavelength dependence with increased HAB for aggregates along the flame wing.

2 Sampling and optical diagnostics

2.1 Thermophoretic sampling particle diagnostic for f_v

TSPD is a powerful technique for the ex situ characterization of in-flame sampled soot using electron microscope analysis. The method is based on the work of Eisner and Rosner [32] and was adapted by Köylü et al. [31] to determine soot volume fraction using the flat plate geometry commonly applied for thermophoretic sampling of soot. In each TEM image, the mass flux of particles ($\dot{m}''$) to the grid is given by

$$\dot{m}'' = \frac{\rho V_p}{A_i \sigma} \tag{1}$$

where ρ is the soot density, V_p is the total particle volume, A_i is the image area, and σ is the grid exposure time. The thermophoretic mass flux (j'') [31] to the probe is approximated as

$$j'' \cong D_T \frac{Nu_x}{2x} \left[1 - \left(\frac{T_w}{T_g} \right)^2 \right] \rho f_v \tag{2}$$

and the soot volume fraction is determined by equating Eqs. (1) and (2)

$$f_v \cong \frac{2x V_p}{A_i \sigma D_T Nu_x} \left[1 - \left(\frac{T_w}{T_g} \right)^2 \right]^{-1} \tag{3}$$

where x is the distance in the axial direction above the burner from the edge of the probe to the center of the TEM grid, D_T is the thermophoretic diffusivity, Nu_x is the Nusselt number, T_w is the probe temperature, and T_g is the local gas temperature.

A previously detailed pneumatic sampler and sample tongues [11] were used to apply the TSPD technique, and the system is reviewed here. The sample tongue insertion and extraction times were characterized with a mean time of 7.5 ms. Radial vibration of the sample probe was determined to be <400 μm, and displacement in the axial direction was <300 μm. Samples were acquired through a slot in a piece of acrylic to block perturbations to the flame as a result of the sliding rail's motion. For data collected in this study, the sample tongues (254 μm thick) did not use a washer to hold the TEM grid as in Ref. [11] since the grids were adhered directly to the surface of the tongue with a very small amount of epoxy. This was done to approximate the flat plate geometry of the thermophoretic sampling particle diagnostic [31]. Sample tongues were 4 mm tall at the location of the grid and 2.54 cm tall where the tongue was adhered to the sliding rail. This was done to minimize the volume of the tongue that entered the flame while maximizing sample tongue contact with the sliding rail to minimize vibration. The sample tongues were inserted directly into the flame and were imaged at 3 kHz using a Vision Research Phantom v7.3 detector (140 μs exposure) to calculate the grid exposure time. The 200 mesh copper TEM grids had a thin coating (5–6 nm) of pure carbon (EMS, CF200-CU) and were analyzed on a 200 kV FEI Tecnai Osiris TEM. For each sample, 45 images were taken at 6300× and 26500× magnification. The relations for thermophoretic diffusivity, gas kinematic viscosity, and Nusselt number from Ref. [31] were used in this study along with the value for T_w (350 K). The probe wall temperature was not measured in this study and increases with increased grid exposure time (see Appendix 1). The local gas temperatures were determined in a previous study [10], x was equal to 2 mm, and the local gas velocities in the axial direction (u_x, ranging from 1.5 m/s to 2.4 m/s) were taken from numerical simulations [2].

The remaining parameter needed to solve Eq. (3) is the volume of particles contained in each image. The method used in Ref. [31] to determine the volume of particles per image is based on image segmentation. The number of primary particles per aggregate (N) is related to the two-dimensional projected aggregate area (A_a) and mean projected primary particle area (A_p) according to Eq. (4), where $\alpha = 1.155$ and $k_a = 1.095$ are empirical constants [33].

$$N = k_a \left(\frac{A_a}{A_p} \right)^{\alpha} \tag{4}$$

Assuming no primary particle overlap, this implies that the total volume of particles is given by (5).

$$V_p = \frac{\pi d_p^3}{6} \sum_l N_l \tag{5}$$

The image segmentation process detailed in Ref. [11] is used here to determine d_p, A_p, and A_a. Processing of the raw TEM images was done in MATLAB, and primary particle diameters were calculated using a Hough transformation along with user input to identify improper primary particle selection by the algorithm. The projected primary particle area was determined from the mean primary particle diameter at each sample location. The projected aggregate area was determined using a Canny edge detection algorithm after binning the image 2×2.

Since flame-generated soot aggregates are known to have particle overlap, Eq. (5) may overpredict the volume of particles. As a result, an additional method to calculate the volume of soot particles, developed by Tian et al. [34, 35], was used to provide an independent measure of V_p. Their method is based on the relative optical density (ROD) of soot in TEM images, which results from electron extinction through aggregates with different thicknesses. They showed that the depth of a soot particle in the direction of the optical path at a given pixel location (x, y) is proportional to the relative optical density, which is defined in Eq. (6)

$$D_{\text{relative}}(x, y) = -log\left(\frac{I(x, y)}{I_{\text{background}}}\right) \tag{6}$$

where $I(x, y)$ is the intensity at pixel location (x, y) and $I_{\text{background}}$ is a scalar value determined for each image by calculating the mean intensity from a region in the image not containing soot. $I_{\text{background}}$ accounts for extinction due to the thin carbon film. The volume of soot particles is related to the summation of the relative optical density over all the pixels in an image through a calibration constant C, as in Eq. (7) where δA is the area projected onto a pixel.

$$V_p = C \sum_{x,y} D_{\text{relative}}(x, y)\delta A \tag{7}$$

The calibration constant is determined using Eq. (7) by measuring the relative optical density of isolated primary particles [34]. The isolated primary particles are assumed to have a spherical geometry, which allows C to be determined by measuring the particle diameter (used to calculate volume) and the summation of its relative optical density over the sphere's projected area. It is difficult to assess the uncertainty associated with calculating V_p and subsequently f_v. Therefore, image segmentation and ROD are both utilized to calculate the volume of particles since their independence should highlight any major discrepancies between the two approaches.

The Santoro burner was used in this study to validate our implementation of the TSPD technique through comparison to previous work on flow condition 1 (NS) [31, 36]. The TSPD technique was then applied at targeted locations in the Yale coflow diffusion burner, which consists of a 4-mm-inner-diameter (I.D.) fuel tube that is concentric with a 74-mm-I.D. coflow of air exiting a honeycomb mesh with 0.8-mm cells. The average fuel-tube exit velocity (parabolic velocity profile) and coflow exit velocity (plug velocity profile) are matched at 35 cm/s. The fuel source is ethylene diluted with nitrogen, and the flames are designated by the volumetric fuel percentage (40, 60, and 80 %) of the total flow rate. This provides flames with different soot loading and particle temperature–time histories. Results are presented in Sect. 3.

2.2 Scattering-to-absorption ratio using thermophoretic sampling/TEM analysis

The scattering-to-absorption ratio, which is one of the two components of the soot extinction coefficient, can be calculated using RDG-FA theory. We followed the approach detailed in Ref. [10], and the calculation is outlined here. Equation (8) defines the scattering-to-absorption ratio as the total aggregate scattering cross section divided by the total aggregate absorption cross section.

$$\begin{aligned}
\rho_{SA}(\lambda) &= \frac{\sigma_{\text{sca}}^{\text{agg}}}{\sigma_{\text{abs}}^{\text{agg}}} \\
&= \frac{M_2/M_1}{\left(M_{2+2/D}/M_2\right)^{D/2}} \\
&\quad \times \frac{\frac{2}{3}N_{eff}k^3\left(d_p/2\right)^6 F(m)\left(1 + \frac{4}{3D}k^2R_{g,\text{eff}}^2\right)^{\frac{-D}{2}}}{E(m)\left(d_p/2\right)^3}
\end{aligned} \tag{8}$$

$$M_i = \int_{N=1}^{N=\infty} n(N)N^i dN \tag{9}$$

The distribution moments (M_i) are defined in Eq. (9) where $n(N)$ is the aggregate number density distribution. N_{eff} is defined as $N_{eff} = k_0 \left(2 \cdot R_{g,\text{eff}}/d_p\right)^D$ where k_0 is the fractal prefactor, $R_{g,\text{eff}}$ is the effective radius of gyration, d_p is the primary particle diameter, and D is the fractal dimension. The wave vector in Eq. (8) is defined as $k = 2\pi/\lambda$, and the ratio of scattering-to-absorption functions ($F(m)/E(m)$) was taken from Ref. [22] as a second order polynomial fit over wavelength. Although the relation for the scattering-to-absorption functions was not derived from the in-flame aggregates of interest, the same relation was used in Ref. [20] since the calculated soot absorption function is a weak function of $F(m)/E(m)$. Thermophoretic sampling data

acquired in Ref. [11] were processed using TEM analysis to calculate the distribution moments, N_{eff}, d_p, D, $R_{g, eff}$, and k_0.

The uncertainty associated with an RDG-FA calculation of $\rho_{SA}(\lambda)$ is difficult to assess due to the myriad of details that go into thermophoretic sampling and TEM analysis. Therefore, as is commonly done [30], we assume that the uncertainty in $\rho_{SA}(\lambda)$ is no less than 10 % due to the often cited 10 % accuracy of RDG-FA theory [23] used to calculate the aggregate scattering and absorption cross sections.

2.3 Soot absorption function based on spec-LOSA

The soot absorption function is derived experimentally from Eq. (10)

$$f_v = \frac{-\ln(\tau)\lambda}{K_{ext}L} = \frac{-\ln(\tau)\lambda}{6\pi L(1 + \rho_{SA}(\lambda))E(m)} \tag{10}$$

where τ is light transmission and L is the path length through the sample. Spectrally resolved light transmission data are utilized along with a TSPD-derived soot volume fraction and $\rho_{SA}(\lambda)$ calculated using RDG-FA theory with data from previous thermophoretic sampling [11] to determine $E(m)$. Spec-LOSA data were obtained previously [10], and the experimental procedure is outlined here. A low spatial coherence white light source (Dolan-Jenner Fiber-Lite series 180) was used for illumination. Light from the source was collected through a 2-mm-diameter aperture and collimated with a 200-mm-focal-length spherical lens and directed through the flame. The transmitted light was collected with a 125-mm-focal-length spherical lens before being focused through an aperture and being re-collimated with a 125-mm-focal-length spherical lens. The resulting collimated light was directed onto the 0.05-mm entrance slit of an imaging spectrograph (Jobin–Yvon CP200, 200-groove/mm grating). The dispersed light was imaged with a thermoelectrically cooled CCD detector (SBIG STF-8300 M chip, 16 bits/pixel digitization, 3326 × 2504, 5.4 µm pixel length) that was stabilized at −10 °C to reduce thermal noise. The images contained a spatial coordinate that spanned the flame radius (5.95 µm projected onto each pixel) and a spectral coordinate that spanned 400 nm to 750 nm (0.14 nm per pixel). The burner was mounted on a stepper motor, and transmission (flame on, lamp unblocked) and emission (flame on, lamp blocked) images were collected every 0.5 mm starting at 1 cm HAB. Transmission images were calculated at each HAB by taking the difference between the transmission and emission images and dividing by the difference between a lamp (lamp on, flame off) image and a dark (lamp off, flame off) image.

The soot dispersion exponent can be found through a spectrally resolved light extinction experiment and information about particle morphology [10]. The scalar dispersion values can also be related to data from two-excitation-wavelength LII (ratio of soot absorption functions, [37]), which is often used to determine $E(m(\lambda_1))/E(m(\lambda_2))$. This is shown in Eqs. (11) and (12), where the soot absorption coefficient ($K_{abs, \lambda}$) is proportional to the inverse of wavelength to the α power. From this, it is implied that the soot absorption function is proportional to the inverse of wavelength to the (α-1) power.

$$K_{abs,\lambda} = \frac{6\pi E(m)f_v}{\lambda} \propto \frac{1}{\lambda^\alpha} \Rightarrow E(m) \propto \frac{1}{\lambda^{\alpha-1}} \tag{11}$$

If the ratio of the soot absorption function at any two excitation wavelengths is taken, as in Eq. (12), it is equal to the inverse of the respective wavelength ratio taken to the (α-1) power. Therefore, Eq. (12) is able to relate a measurement of the soot dispersion exponent from spec-LOSA and thermophoretic sampling/TEM analysis to data from two-excitation-wavelength LII.

$$\frac{E(m(\lambda_1))_\alpha}{E(m(\lambda_2))_\alpha} = \left(\frac{\lambda_2}{\lambda_1}\right)^{\alpha-1} \tag{12}$$
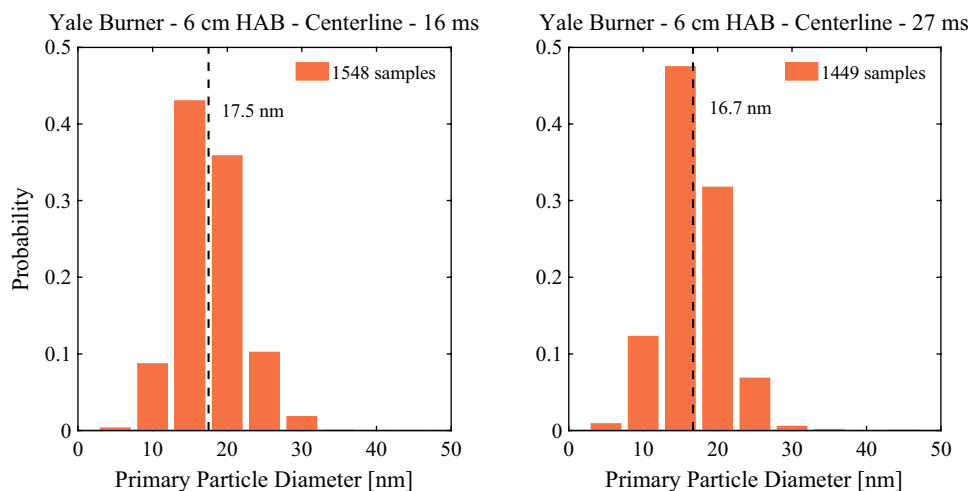
3 Results and discussion

3.1 Thermophoretic sample exposure

The TSPD-derived soot volume fraction must be free of exposure-dependent sampling artifacts since it is proportional to the volume of sampled particles and inversely proportional to the grid exposure as seen in Eq. (3). Previous studies have shown possible oxidative effects with increased sample exposure [38]. Growth effects may also be possible depending on the sample substrate material, geometry, and measurement environment [39]. However, other studies did not observe morphological changes with different exposures [11, 40]. In this work, samples were taken with multiple exposures at two locations in the 80 % flame. The first sample was acquired at 6 cm HAB along the flame centerline to investigate oxidative effects. Previous studies measured high temperature (~1700 K) [10] at this location, and computational results indicate the presence of oxidative species [2]. Primary particle diameters were measured for samples taken with exposures of 16 and 27 ms; the resulting histograms are shown on the left and right of Fig. 1, respectively. Both histograms list the number of sampled primary particles, and a dashed line is drawn with a label to indicate the mean diameter. Within measurement uncertainty, no oxidative effects were observed and thus the measured f_v is assumed to be independent of sample time.
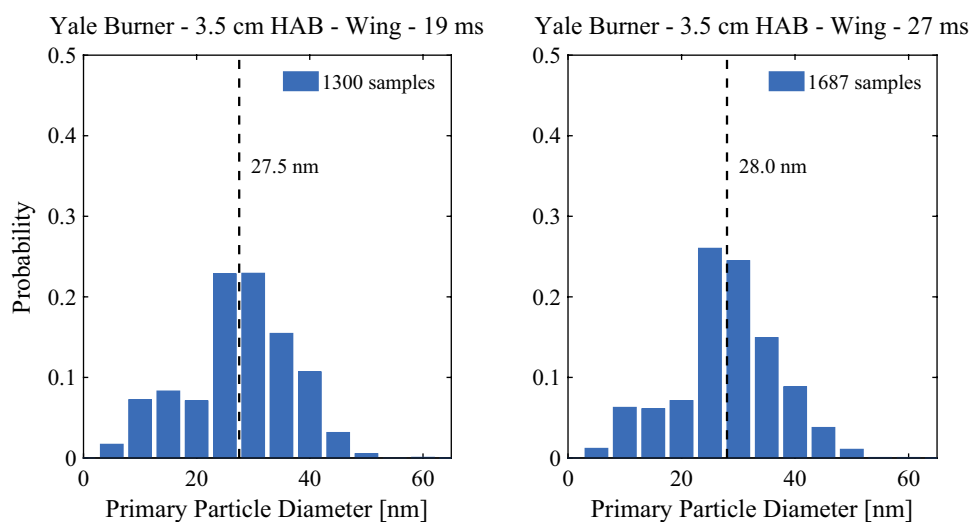
A similar procedure was used along the wing in the 80 % flame at 3.5 cm HAB, where temperatures are high (~1800 K, [10]) and previous computational results indicate the presence of surface growth species such as acetylene

Fig. 1 Primary particle diameter measured for sample exposures of 16 and 27 ms along the centerline at 6 cm HAB in the 80 % flame

Yale Burner - 6 cm HAB - Centerline - 16 ms

17.5 nm

1548 samples

Yale Burner - 6 cm HAB - Centerline - 27 ms

16.7 nm

1449 samples

Fig. 2 Primary particle diameter measured for sample exposures of 19 and 27 ms along the wing at 3.5 cm HAB in the 80 % flame

Yale Burner - 3.5 cm HAB - Wing - 19 ms

27.5 nm

1300 samples

Yale Burner - 3.5 cm HAB - Wing - 27 ms

28.0 nm

1687 samples

[2]. This sample location was selected to consider the possibility of particle growth with sample time. Primary particle diameter distributions are shown in Fig. 2 for sample times of 19 and 27 ms. The number of sampled particles is listed in each histogram, and a dashed line is drawn and labeled to indicate the mean diameter. No change in the distributions is observed, and the sampled f_v is assumed to be independent of growth effects.

In contrast to Refs. [38, 39], no sample artifacts were observed with an increase in sample time. However, sample times were purposely minimized to avoid aggregate overlap by keeping the grid coverage of aggregates <20 %. The sample times used in this study are small compared to other studies [11, 38] because the TEM grid was not recessed into the sample tongue, which increases the flux of particles to the grid per unit time [11]. In addition, primary particle diameter was measured in Ref. [11] at the same locations in the 80 % flame for exposures of ~120 and ~80 ms, respectively. The longer sample times were possible due

to a recessed TEM grid, and the measured primary particle diameters are consistent with the results presented here. Thus, sample artifacts were not observed under the given flow conditions.

3.2 Soot volume fraction

The volume of particles in each image was determined using image segmentation (6300×) and relative optical density (26500×) techniques as discussed in Sect. 2.1. For each technique, the volume of particles was determined from the average of 45 images and example data are shown in Fig. 3 (80 % flame, 3.5 cm HAB, wing). On the left is the 8-bit raw TEM image, where each aggregate has been segmented and outlines are set to 255 counts. On the right is a relative optical density image of soot from the same sample. The image background contains zero mean value noise that does not contribute to the summation of the relative optical density in each image.
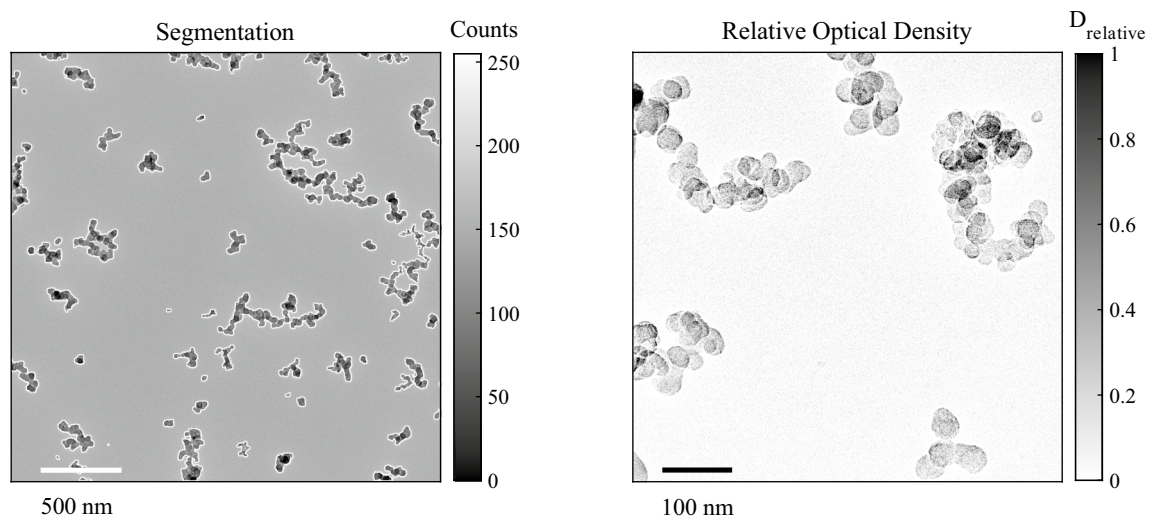
Fig. 3 Image segmentation (*left*, 6300×) and relative optical density (*right*, 26500×) images used to determine the volume of soot aggregates

Table 1 Soot volume fraction and parameters used in the thermophoretic sampling particle diagnostic

Sample	Location	Percent grid coverage	Grid exposure (ms)	Axial velocity (m/s)	Gas temperature (K)	f_v Seg. (ppm)	f_v ROD (ppm)	f_v ave. (ppm)
5 cm HAB Santoro	Centerline $r = 0$ mm	19	39	1.0	1580	3.4	3.1	3.3
2 cm HAB Yale	Wing $r = 3.3$ mm	16	38	1.5	1750	1.7	1.9	1.8
3.5 cm HAB Yale	Wing $r = 2.6$ mm	15	19	1.9	1800	3.6	4.3	3.8
	Wing $r = 2.6$ mm	19	27	1.9	1800	3.4	3.9	
6 cm HAB Yale	Centerline $r = 0$ mm	14	16	2.4	1680	2.1	2.2	2.1
	Centerline $r = 0$ mm	19	27	2.4	1680	1.8	2.1	

The TSPD technique was initially applied in the Santoro burner at 5 cm HAB along the flame centerline to validate our application of the TSPD technique through comparison to data from the original study [31]. The first row of Table 1 lists the parameters used in Eq. (3) to calculate the soot volume fraction with image segmentation and ROD. The last column contains the mean f_v derived using image segmentation and ROD over all grid exposures at a given measurement location. A value of 3.3 ppm was determined in the Santoro burner using the same velocity and gas temperature as Ref. [31], which compares well with the ≈3.8 ppm determined in the original study. This value also compares well with previous LII work in our laboratory at this measurement location that yielded 2.5–3.9 ppm, depending on the value of the selected soot extinction coefficient (K_{ext} = 8.6–5.5) [41].

The remaining samples were taken in the 80 % flame on the Yale burner and are listed in Table 1. The axial gas velocity was taken from previous computations [2], and the local gas temperature was measured in Ref. [10] using color ratio soot pyrometry with a measured soot dispersion exponent. Despite the fact that the image segmentation technique assumes no primary particle overlap, the results are consistent with the ROD method at all measurement locations.

3.3 Soot optical properties

Without knowledge of soot optical properties for specific flow conditions, a common practice is to assume an extinction coefficient derived from a GSLE experiment. Recent studies utilized a soot extinction coefficient of
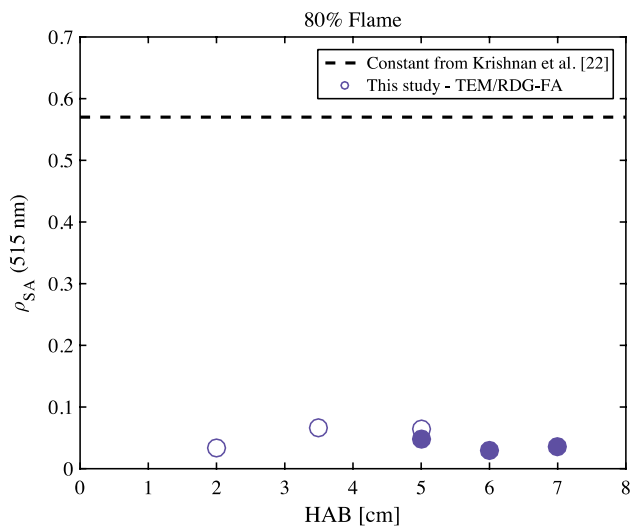
Fig. 4 Soot scattering-to-absorption ratio constant from over-fire soot in Ref. [22] and those calculated using RDG-FA theory and information from thermophoretically sampled aggregates acquired in Ref. [11] in the Yale burner. The *open circles* were acquired along the flame wing, and the *filled circles* were acquired along the flame centerline

8.6 ([18], consistent with [22]) to determine soot volume fraction from LII and two-color ratio pyrometry in the Yale burner [12]. The techniques compare well and suggest that the accuracy of the recovered soot volume fraction is not limited by available diagnostics but by the accuracy of the known soot optical properties. No information about $E(m)$ or $\rho_{SA}(\lambda)$ is given in [18], but the extinction coefficient derived in Ref. [22] at 515 nm is comprised of $E(m(515 \text{ nm})) = 0.29$ and ρ_{SA} (515 nm) ≈ 0.57. As noted in Sect. 2.2, $\rho_{SA}(\lambda)$ can be calculated through RDG-FA theory using information about soot morphology derived from thermophoretic sampling and electron microscope analysis. Soot samples at six locations in the 80 % flame were previously acquired in Ref. [11], and the morphology information is used here to calculate $\rho_{SA}(515 \text{ nm})$, since the sparse grid coverage (<10 %) of the samples ensures reliable information about morphology and size distributions. The three TSPD sample locations are a subset of the sample locations in Ref. [11]. The calculated scattering-to-absorption ratios are plotted in Fig. 4 along with the constant $\rho_{SA}(515 \text{ nm}) = 0.57$ from Ref. [22].

Equation (8) was used to calculate $\rho_{SA}(\lambda)$ and accounts for polydispersity effects due to the number of primary particles per aggregate, but does not account for the distribution of primary particle diameters. The assumption of a monodisperse primary particle diameter distribution is common and requires discussion. Instead of $\rho_{SA}(\lambda)$ being proportional to $(d_p/2)^3$ for the monodisperse case, as is suggested by Eq. (8), the actual proportionality is to the sixth moment of the primary particle distribution divided by the

third moment of the primary particle distribution. The data in Figs. 1 and 2 were numerically evaluated to determine the normalized sixth moment of the primary particle distribution divided by the normalized third moment of the primary particle distribution, where the Rth normalized moment of the distribution is defined as the Rth moment of the distribution divided by the mean value of the distribution taken to the Rth power. For the centerline and wing soot samples, this ratio was found to be 1.9 and 2.3, respectively. Therefore, Eq. (8) under predicts $\rho_{SA}(\lambda)$ by approximately a factor of 2 when assuming a monodisperse distribution. However, this is not the complete story as the ratio of scattering-to-absorption functions ($F(m)/E(m)$), taken from Ref. [22], was derived under the assumption of a monodisperse primary particle distribution. The function can be modified to account for primary particle diameter polydispersity by assuming a distribution and width parameter, given a mean primary particle diameter of 42 nm from the listed values in Ref. [22]. Previous studies by Köylü and Faeth [42] and Snelling et al. [25] found width parameters between 1.2 and 1.3 for lognormal distributions. For the data presented in Figs. 1 and 2, lognormal width parameters of 1.3 and 1.5 were determined, respectively. The quality of the lognormal fit to the centerline data was excellent, while the quality of the lognormal fit to the wing data was poor. Therefore, we can correct the ratio of scattering-to-absorption functions by assuming a lognormal distribution and a universal width parameter of 1.3 for the centerline data only. Doing so results in an approximately 60 % reduction in the $F(m)/E(m)$ ratios reported in Ref. [22]. Taken together, the 60 % reduction and factor of 1.9 increase results in an approximately 20 % net reduction in the $\rho_{SA}(\lambda)$ values shown in Fig. 4. For centerline soot, where the primary particle diameters follow a lognormal distribution, this results in a < 2 % change in $E(m)$ based on Eq. (10). Although this argument does not hold for soot collected along the flame wing (not a lognormal distribution), the effects of primary particle diameter polydispersity are ignored in this study based on the moderate reduction in $\rho_{SA}(\lambda)$ and negligible change to $E(m)$.

For all plots, the open markers were acquired along the flame wing and filled markers were acquired along the flame centerline. The results in Fig. 4 show an order of magnitude decrease between the scattering-to-absorption ratios in the turbulent post-flame soot and the laminar coflow in-flame soot, respectively. This is likely due to the increase in size and primary particle diameter of aggregates found in the over-fire turbulent diffusion flame ($N_{ave} \sim 400\text{--}500$, $d_p \sim 30\text{--}50$ nm) [22] compared to those found in the Yale coflow burner ($N_{ave} \sim 20\text{--}120$, $d_p \sim 15\text{--}30$ nm) [11]. The relative contribution to scattering is increased for the over-fire aggregates because Eq. (8) is proportional to N_{eff} and is also a strong function of primary particle diameter. Thus, although K_{ext} is not a strong function of $\rho_{SA}(\lambda)$, the strong
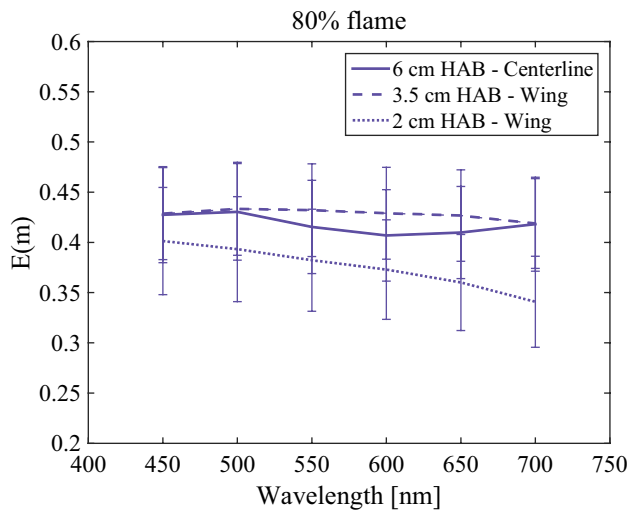
80% flame

Fig. 5 Soot absorption function calculated as a function of wavelength using Eq. (10) at three locations in the 80 % flame with light transmission data from a spec-LOSA experiment [10], soot volume fraction from TSPD (this study), and the soot scattering-to-absorption ratio calculated in this study with morphological data obtained in Ref. [11]

morphology dependence of $\rho_{SA}(\lambda)$ must be considered when selecting optical parameters to determine soot volume fraction in LII or two-color ratio pyrometry experiments.

The absorption function is the remaining component of K_{ext} and can be determined once $\rho_{SA}(\lambda)$ is calculated. Surveys of values found in the literature [20, 43] show a range of values ($E(m) \approx 0.10$–0.40) in the visible portion of the spectrum. Various arguments have been put forward [22, 43] to narrow the range of usable soot absorption functions, but significant uncertainty persists.

The soot absorption function can be calculated as a function of wavelength using Eq. (10), and the results are plotted in Fig. 5 (50-nm intervals) for the three TSPD sample locations in the 80 % flame. Uncertainty bars were calculated as detailed in the Appendix and are included in Fig. 5. The soot absorption function appears to have a wavelength dependence, which will be investigated further in Sect. 3.4. Table 2 contains values of the soot absorption function from in-flame measurements in coflow laminar diffusion flames in addition to the values from Fig. 5 at 532 and 635 nm at the three measurement locations. The literature values are from a variety of independent techniques such as the previously mentioned LII-derived soot absorption function of 0.4 determined by Snelling et al. [25]. Using a modulated LII technique, Snelling et al. [44] determined $E(m) = 0.45$ in the visible portion of the spectrum. In the first in-flame GSLE measurement of K_{ext}, Williams et al. [19] measured $K_{ext} = 9.3$ ($\rho_{SA}(635\ nm) = 0.11$–$0.21$), $K_{ext} = 9.7$ ($\rho_{SA}(635\ nm) = 0.17$–$0.30$), and $K_{ext} = 6.5$ ($\rho_{SA}(635\ nm) < 0.03$) at 635 nm for ethylene, kerosene, and methane flames, respectively. The range of the soot absorption function listed in Table 2 for [19] was determined from the mean extinction coefficient and the range of scattering-to-absorption values. Thus, although the uncertainty of $E(m)$ calculated in this study is ± 11–14 %, the values are in excellent agreement with the body of available in-flame measurements of $E(m)$ in similar coflow laminar diffusion flames.

Figure 6 shows soot volume fraction derived from TSPD (diamonds) and extinction data [10] (squares) calculated using Eq. (10) at $\lambda = 515$ nm with $K_{ext} = 8.6$ from Ref. [22]. An uncertainty analysis by error propagation for the TSPD-derived soot volume fraction was conducted

Table 2 Soot absorption functions from in-flame measurements in laminar coflow diffusion flames

	$E(m)$	λ (nm)	Diagnostic	Burner	Fuel
Snelling et al. [25]	0.4	532	LII/LII modeling	Gülder burner	Ethylene
Snelling et al. [44]	0.45 ± 0.04	465	Modulated LII	Gülder burner	Ethylene
	0.45 ± 0.03	577			
	0.42 ± 0.02	865			
This work					
2 cm HAB	0.38 ± 0.05	532	TSPD/spec-LOSA	Yale burner	Ethylene
3.5 cm HAB	0.43 ± 0.05	532			
6 cm HAB	0.42 ± 0.05	532			
Williams et al. [19]	0.41–0.44	635	In-flame GSLE	Similar to Santoro burner	Ethylene
Williams et al. [19]	0.40–0.44	635	In-flame GSLE	Similar to Santoro burner	Kerosene
Williams et al. [19]	0.34	635	In-flame GSLE	Similar to Santoro burner	Methane
This work					
2 cm HAB	0.36 ± 0.05	635	TSPD/spec-LOSA	Yale burner	Ethylene
3.5 cm HAB	0.42 ± 0.05	635			
6 cm HAB	0.40 ± 0.05	635			
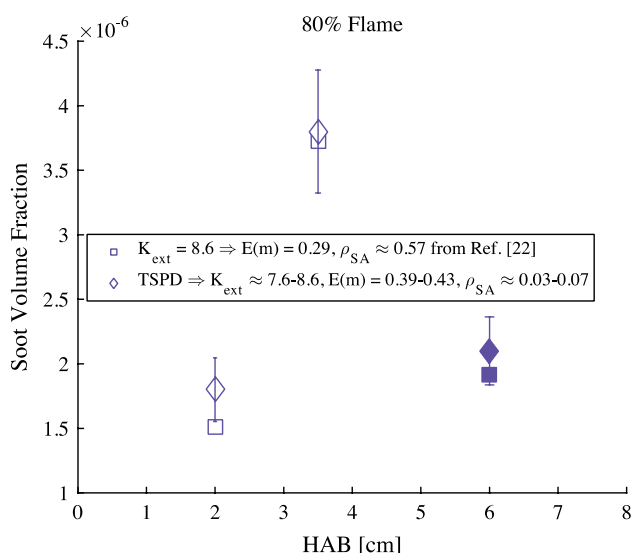
Fig. 6 Soot volume fraction calculated using TSPD (*diamonds*) and light extinction at 515 nm using $K_{ext} = 8.6$ (*squares*). The TSPD soot volume fraction is used with the calculated scattering-to-absorption ratios (data from Ref. [11]) along with spec-LOSA data [10] to determine an extinction coefficient and soot absorption function. The *open markers* were acquired along the flame wing, and the *filled markers* were acquired along the flame centerline

(see Appendix 1). Error bars are included for the TSPD soot volume fraction with uncertainties of ± 14, ± 12, and ± 13 % for the 2, 3.5, and 6 HAB sample locations, respectively. Although only a moderate (<15 %) difference in soot volume fraction is observed compared to previous studies in the Yale burner [2, 12], the apparent accuracy derived from using $K_{ext} = 8.6$ [22] was due to the relative cancelation of an $E(m)$ that was too small and a $\rho_{SA}(\lambda)$ that was too large for aggregates in the 80 % flame. Thus, the morphology dependence of soot optical properties requires specific knowledge of soot in the reacting flow under investigation. For laboratory-scale flames designed for combined experimental and computational research, detailed knowledge of soot morphology is needed to provide accurate experimental data for comparison to model results.

3.4 Soot absorption function ratio

The value of the soot absorption function at specific wavelengths was determined in the previous section, but modest wavelength dependence is apparent in Fig. 5. The wavelength dependence of the soot absorption function is contested, with available data suggesting both a non-constant [21, 45, 46] and constant dependence [20, 25, 26, 29] over the visible portion of the spectrum.

Spectrally resolved extinction data in the 40, 60, and 80 % flames were selected over a subset (450–700 nm) of the total spectral region to improve the dispersion exponent fit in low signal-to-noise regions of the flame. The path-integrated extinction data were inverted using Tikhonov regularization and an onion-peeling discretization to reduce noise propagation compared to an Abel three-point inversion [47]. The regularization parameter was selected by inspecting the singular values of the augmented onion-peeling matrix [48]. Regularization is beneficial due to the weaker extinction signals and subsequently lower signal-to-noise ratios in the 40 and 60 % flames compared to the 80 % flame. The inverted hyperspectral images were smoothed in the spectral direction with a LOESS algorithm, which improved the signal-to-noise ratio but did not affect the calculated dispersion exponent.

The wavelength dependence of the soot absorption function derived from spec-LOSA is susceptible to interference from the wavelength dependence of absorption by soot precursors. Leschowski et al. [49] investigated the influence of soot precursors on a spec-LOSA experiment in the Gülder burner and demonstrated a wavelength dependence for soot precursor absorption at shorter particle residence times compared to mature soot aggregates where soot precursor absorption was not spectrally dependent. Therefore, for mature soot aggregates in this study, we assume a negligible contribution to the wavelength dependence of the spec-LOSA data from soot precursor absorption.

The α map for the 80 % flame, presented in [10], was found by fitting the extinction (α_{ext}) and scattering (α_{sca}) data separately as a function of wavelength and taking the difference to determine α. In Ref. [10, 11], the wavelength dependence of the scattering component was found to be small compared to the contribution from absorption (see supplemental information in Ref. [11]). At the six sample locations in the 80 % flame listed in Fig. 4, α_{sca} was calculated to be in the range of 0.02–0.05. As a result, a constant $\alpha_{sca} = 0.035$ was subtracted from the two-dimensional map of α_{ext} with an expected error of <3 % in α at all data points. This was done to determine the soot dispersion coefficient for the three flow conditions presented in Fig. 7.

The majority of data points presented in each flame correspond to $\alpha \approx 1.2$. Thus, the presented data indicate a negative exponential wavelength dependence for the soot absorption function over the visible portion of the spectrum that goes approximately as $\lambda^{-0.2}$. In contrast, soot along the wings of the 80 % flame is noted to have a dependence on wavelength that varies as a function of HAB ($\lambda^{-0.2}$–$\lambda^{0.1}$), where the soot at 2 cm HAB has a similar dependence to that of the centerline soot ($\alpha \approx 1.2$). The dispersion
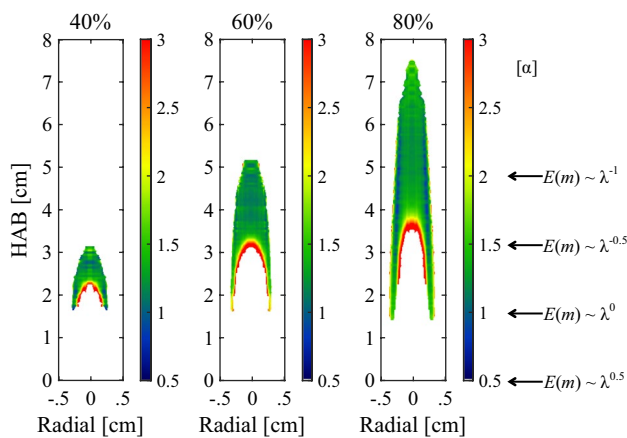
Fig. 7 Measured soot dispersion exponent in the 40, 60, and 80 % flames determined with data from a spec-LOSA experiment [10] and morphological information from Ref. [11]

Fig. 8 Measured soot absorption function ratio $E(m(450\ nm))/E(m(700\ nm))$ in the 40, 60, and 80 % flames calculated with data from a spec-LOSA experiment [10] and morphological information from Ref. [11]

exponent decreases along the wing with increased HAB, which also spatially coincides with an increased mean primary particle diameter [11] and results in a change from a negative to positive exponential wavelength dependence. The changing wavelength dependence can be seen between the 2 and 3.5 cm HAB samples in Fig. 5. The positive $\lambda^{0.1}$ dependence of the soot absorption function along the wings in the 80 % flame is consistent with that stated by Michelsen et al. [46] ($\lambda^{0.17}$) at 5 cm HAB along the wing of the Santoro burner. However, it is noted that temperature-dependent effects on soot optical properties may be present in LII experiments due to laser heating [46]. Thus, the alpha map for the 80 % flame shows that depending on the in-flame location of soot aggregates, there may be positive or negative exponential wavelength dependence for the soot absorption function. This conclusion is consistent with the varied wavelength dependencies stated in the literature over a range of reacting flows and particle morphologies [20, 43, 45, 50].

Equation (12) was used to convert the alpha maps from Fig. 7 to the ratio of soot absorption functions at 450 and 700 nm, and the results are plotted in Fig. 8 for the 40, 60, and 80 % flames. The centerline soot in each flame, for mature aggregates, has a ratio of ≈1.1, which is close to the ≈1.1 determined in Ref. [30] for 450 and 750 nm along the centerline in a similar coflow diffusion burner. The results in Fig. 8 show that the ratio of absorption functions is relatively invariant to age (HAB) [30] or spatial location in the 40 and 60 % flames (for mature aggregates), in addition to along the centerline in the 80 % flame (for mature aggregates). Along the wings in the 80 % flame, where the morphology is known to be different than along the
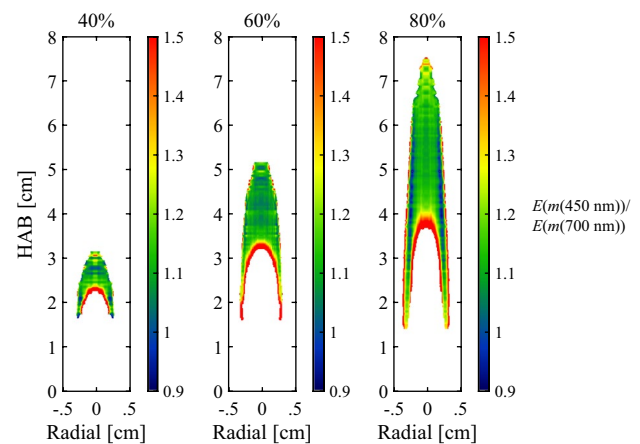
centerline [11], the ratio is observed to be lower (≈0.95 at 5 cm HAB). This is consistent with Ref. [37] where soot absorption cross-sectional ratios were observed to be larger along the centerline than the wing in the Santoro and Gülder burners. For young soot aggregates, at the lowest HAB along the centerline and wing the ratio is much larger, indicating a stronger relative absorption at shorter wavelengths. These conclusions are consistent with observations in Ref. [30, 51], but it should be noted that the accuracy of α at these locations could be affected by spectrally dependent absorption from soot precursors [49].

4 Conclusions

The soot absorption function and scattering-to-absorption ratio are important to the optical study of in-flame soot and to post-flame modeling of climate forcing from soot. This study focused on in-flame soot optical properties in the Yale coflow diffusion burner to validate the accuracy of experimental soot volume fraction for comparison to results from numerical models.

The TSPD technique was used to provide an in-flame measurement of soot volume fraction in the 80 % flame at three locations. Samples were taken with two different grid exposures at two locations to investigate possible oxidative or growth effects. No such effects were observed. The volume of soot particles in a TEM image was calculated using image segmentation and ROD, which were found to give consistent results.

The TSPD soot volume fraction was compared to soot volume fraction derived using light extinction data from a previous experiment [10] along with $K_{ext} = 8.6$ from Ref. [22]. There was only a modest difference (<15 %) between the soot volume fraction derived using $K_{ext} = 8.6$ from Ref. [22] and the TSPD soot volume fraction. This is despite the fact that $\rho_{SA}(515 \text{ nm}) \approx 0.57$ and $E(m(515 \text{ nm})) = 0.29$ for the post-flame soot in Ref. [22], while $\rho_{SA}(515 \text{ nm}) \approx 0.03$–$0.07$ and $E(m(515 \text{ nm})) = 0.39$–$0.43 \pm 0.05$ were determined for in-flame soot. The soot absorption function derived in this study was found to be in very good agreement with the body of independent in-flame measurements of $E(m)$ in similar coflow laminar diffusion flames [19, 25, 27].

The wavelength dependence of the soot absorption function was found at additional flow conditions (compared to Ref. [10]) through data from a previous spec-LOSA experiment [10] and was improved through Tikhonov regularization compared to an Abel three-point inversion. The wavelength dependence of scattering from soot was approximated as a constant value with negligible additional uncertainty in the calculated soot dispersion exponent. The soot absorption function along the wing of the 80 % flame was found to change from a positive to negative exponential wavelength dependence with increasing HAB. Otherwise, mature soot aggregates were found to have $\alpha \approx 1.2$ in the three flames, and younger soot was found to have a larger dispersion exponent. The α maps were converted to the ratio of soot absorption functions at two wavelengths for comparison to two-excitation-wavelength LII data. For mature aggregates in all of the flow conditions, the ratio $E(450 \text{ nm})/E(700 \text{ nm})$ was found to be approximately constant (≈ 1.1), except along the wings of the 80 % flame where a lower ratio was observed (≈ 0.95). However, young soot along the flame wings and centerline was observed to have a larger ratio indicating a stronger relative absorption at shorter wavelengths. These observations are consistent with recent LII studies [25, 30].

Appendix 1: Uncertainty analysis

To assess the uncertainty of the TSPD/spec-LOSA-derived soot volume fraction and absorption functions, an uncertainty analysis was conducted. The uncertainty in f_v was determined by propagating uncertainty from the independent parameters in Eq. (3) as shown in Eq. (13). The uncertainty in V_p, σ, Nu_x, T_w, and T_g was taken to be 6, 4, 10, 10, and 3 %, respectively. Since the probe wall temperature is a function of grid exposure, we include a 10 % uncertainty estimate to span the range of possible temperatures with the 385 K measured in Ref. [40] serving as an approximate upper limit due to their longer grid exposure.

$$\delta f_v = \sqrt{\left(V_p \frac{\partial f_v}{\partial V_p} \frac{\delta V_p}{V_p}\right)^2 + \left(\sigma \frac{\partial f_v}{\partial \sigma} \frac{\delta \sigma}{\sigma}\right)^2 + \left(Nu_x \frac{\partial f_v}{\partial Nu_x} \frac{\delta Nu_x}{Nu_x}\right)^2 + \left(T_w \frac{\partial f_v}{\partial T_w} \frac{\delta T_w}{T_w}\right)^2 + \left(T_g \frac{\partial f_v}{\partial T_g} \frac{\delta T_g}{T_g}\right)^2} \tag{13}$$

Uncertainty in the TSPD-derived f_v was determined from Eq. (13) and used in Eq. (14) to determine uncertainty in the measured soot absorption function. Equation (14) is arrived at after rearranging Eq. (10) and considering uncertainty in τ, $\rho_{SA}(\lambda)$, and f_v to be 1, 10 %, and the result of Eq. (13), respectively.

$$\delta E(m)$$
$$= \sqrt{\left(\tau \frac{\partial E(m)}{\partial \tau} \frac{\delta \tau}{\tau}\right)^2 + \left(\rho_{SA}(\lambda) \frac{\partial E(m)}{\partial \rho_{SA}(\lambda)} \frac{\delta \rho_{SA}(\lambda)}{\rho_{SA}(\lambda)}\right)^2 + \left(f_v \frac{\partial E(m)}{\partial f_v} \frac{\delta f_v}{f_v}\right)^2}$$
$$(14)$$

References

1. T.C. Bond, R.W. Bergstrom, Aerosol Sci. Tech. **40**, 1 (2006)
2. M.D. Smooke, M.B. Long, B.C. Connelly, M.B. Colket, R.J. Hall, Combust. Flame **143**, 4 (2005)
3. T. Blacha, M. Di Domenico, P. Gerlinger, M. Aigner, Combust. Flame **159**, 1 (2012)
4. S.B. Dworkin, J.A. Cooke, B.A.V. Bennett, B.C. Connelly, M.B. Long, M.D. Smooke, R.J. Hall, M.B. Colket, Combust. Theor. Model. **13**, 5 (2009)
5. N.A. Eaves, A. Veshkini, C. Riese, Q.A. Zhang, S.B. Dworkin, M.J. Thomson, Combust. Flame **159**, 10 (2012)
6. K.A. Thomson, M.R. Johnson, D.R. Snelling, G.J. Smallwood, Appl. Optics **47**, 5 (2008)
7. D.R. Snelling, K.A. Thomson, G.J. Smallwood, O.L. Gulder, Appl. Optics **38**, 12 (1999)
8. P.S. Greenberg, J.C. Ku, Appl. Optics **36**, 22 (1997)
9. http://guilford.eng.yale.edu/yalecoflowflames/index.html (06/01/2016)
10. B. Ma, M.B. Long, Appl. Phys. B **117**, 1 (2014)
11. N.J. Kempema, M.B. Long, Combust. Flame **164**, 373 (2016)
12. P. B. Kuhn, B. Ma, B. C. Connelly, M. D. Smooke, M. B. Long, in *Proceedings of the Combustion Institute* **33**, (2011)
13. http://www.adelaide.edu.au/cet/isfworkshop/ (06/01/2016)
14. J. Widmann, J.C. Yang, T.J. Smith, S.L. Manzello, G.W. Mulholland, Combust. Flame **134**, 1–2 (2003)
15. J.F. Widmann, J. Duchez, J.C. Yang, J.M. Conny, G.W. Mulholland, J. Aerosol Sci. **36**, 2 (2005)
16. Z.Q. Zhou, T.U. Ahmed, M.Y. Choi, Exp. Therm. Fluid Sci. **18**, 1 (1998)
17. J.Y. Zhu, A. Irrera, M.Y. Choi, G.W. Mulholland, J. Suo-Anttila, L.A. Gritzo, Int. J. Heat Mass Tran. **47**, 17–18 (2004)
18. M.Y. Choi, G.W. Mulholland, A. Hamins, T. Kashiwagi, Combust. Flame **102**, 1–2 (1995)
19. T.C. Williams, C.R. Shaddix, K.A. Jensen, J.M. Suo-Anttila, Int. J. Heat Mass Tran. **50**, 7–8 (2007)
20. A.R. Coderre, K.A. Thomson, D.R. Snelling, M.R. Johnson, Appl. Phys. B **104**, 1 (2011)
21. S.S. Krishnan, K.C. Lin, G.M. Faeth, J. Heat Transf. **123**, 2 (2001)
22. S.S. Krishnan, K.C. Lin, G.M. Faeth, J. Heat Transf. **122**, 3 (2000)
23. C.M. Sorensen, Aerosol Sci. Technol. **35**, 2 (2001)
24. S. De Luliis, F. Cignoli, G. Zizak, Appl. Optics **44**, 34 (2005)
25. D.R. Snelling, K.A. Thomson, F. Liu, G.J. Smallwood, Appl. Phys. B **96**, 4 (2009)
26. D.R. Snelling, F.S. Liu, G.J. Smallwood, O.L. Gulder, Combust. Flame **136**, 1–2 (2004)
27. V. Beyer, D.A. Greenhalgh, Appl. Phys. B **83**, 3 (2006)
28. E. Therssen, Y. Bouvier, C. Schoemaecker-Moreau, X. Mercier, P. Desgroux, M. Ziskind, C. Focsa, Appl. Phys. B **89**, 2–3 (2007)
29. S. Bejaoui, R. Lemaire, P. Desgroux, E. Therssen, Appl. Phys. B **116**, 2 (2014)
30. F. Migliorini, K.A. Thomson, G.J. Smallwood, Appl. Phys. B **104**, 2 (2011)
31. U.O. Koylu, C.S. McEnally, D.E. Rosner, L.D. Pfefferle, Combust. Flame **110**, 4 (1997)
32. A.D. Eisner, D.E. Rosner, Combust. Flame **61**, 2 (1985)
33. U.O. Koylu, G.M. Faeth, T.L. Farias, M.G. Carvalho, Combust. Flame **100**, 4 (1995)
34. K. Tian, K.A. Thomson, F.S. Liu, D.R. Snelling, G.J. Smallwood, D.S. Wang, Combust. Flame **144**, 4 (2006)
35. K. Tian, F. S. Liu, M. Yang, K. A. Thomson, D. R. Snelling, G. J. Smallwood, in *Proceedings of the Combustion Institute* **31**, (2007)
36. R.J. Santoro, H.G. Semerjian, R.A. Dobbins, Combust. Flame **51**, 2 (1983)
37. X. Lopez-Yglesias, P.E. Schrader, H.A. Michelsen, J. Aerosol. Sci. **75**, 43 (2014)
38. E. Cenker, G. Bruneaux, T. Dreier, C. Schulz, Appl. Phys. B **118**, 2 (2015)
39. L. Figura. Experimental study of incipiently-sooting counterflow flames at high pressures, Ph.D. Thesis, Yale University, 2014
40. R.A. Dobbins, C.M. Megaridis, Langmuir **3**, 2 (1987)
41. B. C. Connelly. Quantitative Characterization of Steady and Time-Varying, Sooting, Laminar Diffusion Flames using Optical Techniques, Ph.D. Thesis, Yale University, 2009
42. U.O. Koylu, G.M. Faeth, Combust. Flame **89**, 2 (1992)
43. C. Schulz, B.F. Kock, M. Hofmann, H. Michelsen, S. Will, B. Bougie, R. Suntz, G. Smallwood, Appl. Phys. B **83**, 3 (2006)
44. D.R. Snelling, R.A. Sawchuk, G.J. Smallwood, K. Thomson, Appl. Phys. B **119**, 4 (2015)
45. J. Yon, R. Lemaire, E. Therssen, P. Desgroux, A. Coppalle, K.F. Ren, Appl. Phys. B **104**, 2 (2011)
46. H.A. Michelsen, P.E. Schrader, F. Goulay, Carbon **48**, 8 (2010)
47. K.J. Daun, K.A. Thomson, F.S. Liu, G.J. Smallwood, Appl. Optics **45**, 19 (2006)
48. K.J. Daun, J. Quant. Spectrosc. Ra. **111**, 1 (2010)
49. M. Leschowski, K.A. Thomson, D.R. Snelling, C. Schulz, G.J. Smallwood, Appl. Phys. B **119**, 4 (2015)
50. H. A. Michelsen, C. Schulz, G. J. Smallwood, S. Will, Prog. Energ. Combust. **51**, 2–48 (2015)
51. G. Cleon, T. Amodeo, A. Faccinetto, P. Desgroux, Appl. Phys. B **104**, 2 (2011)